Effective Wetting Area Based on Electrochemical Impedance Analysis: Hydrophilic Structured Surface

Dejian Zhang[1], *Gyoko Nagayama*[2*]

[1]Graduate School of Engineering, Kyushu Institute of Technology, Sensui 1-1, Tobata, Kitakyushu, Fukuoka 804-8550, Japan

[2] Department of Mechanical Engineering, Kyushu Institute of Technology, Sensui 1-1, Tobata, Kitakyushu, Fukuoka 804-8550, Japan

Corresponding Author:

Gyoko Nagayama

Email: nagayama.gyoko725@mail.kyutech.jp

ABSTRACT: Wettability on nano/microstructured surfaces is gaining remarkable interest for a wide range of applications; however, little is known about the effective wetting area of the solid–liquid interface. In this study, the effect of wettability on electrochemical impedance was experimentally investigated to obtain a better understanding of the effective wetting area. We demonstrate that the water contact angle decreases significantly at hydrophilic surfaces with denser nano/microstructures. Based on the analysis of equivalent electrical circuits, we found that the electrochemical impedance decreases with reducing the water contact angle, showing a dependence on the effective wetting area, i.e., the real solid–liquid contact area. Also, the charge transfer resistance at low frequency was found to be the dominant parameter to estimate the effective wetting area at the solid–liquid interface.

INTRODUCTION

The wettability of solid surfaces has attracted considerable interest since a long period.[1-6] A large number of special wettability materials is being widely used in academic science and industrial technologies.[7-12] Recent advances in microfluidic devices[13-16] and biochips[17-19] have facilitated the fabrication of hydrophilicity and super-hydrophilicity at the solid–liquid interface, where the hydrophilicity and super-hydrophilicity are defined when the water contact angles (WCAs) are smaller than 90° and 5°, respectively.[20]

Physical morphology and chemical composition are important factors that control surface wettability.[21-25] For a static droplet on structured surfaces, Wenzel model describes the state in which the interiors of the surface structures are fully wetted.[26] Conversely, the Cassie–Baxter model describes a completely non-wetted state.[27] An intermediate wetting state between the two classical wetting models, i.e., partial wetting state, has been proposed by Nagayama et al. based

on the molecular dynamics simulation.[28] The effective wetting ratio in the interior of nano/microstructures is applied to the partial wetting model; this ratio is 1 for the fully wetted state and 0 for the non-wetted state. However, in many cases, the experimental water contact angles disagree with either theoretical Wenzel or Cassie–Baxter models[29-31] but correspond well with the partial wetting model for the nano/microstructured surfaces.[32,33] The dependence of the static contact angle on the effective wetting ratio provides evidence that the solid–liquid contact area of the partial wetting state is larger than that of non-wetted state but smaller than fully wetted state. In order to clarify the effective wetting ratio, the $\Phi_s=\Phi+(r_w-\Phi)f$ was applied to show the area ratio of solid–liquid interface to the apparent flat surface, where Φ is the solid fraction, r_w is the surface area increment ratio and f is the effective wetting ratio.[33] Φ_s result in the surface area increment ratio r_w ($=\Phi+(r_w-\Phi)\times 1$ ($r_w \geq 1$)) for the fully wetted state; solid fraction Φ ($=\Phi+(r_w-\Phi)\times 0$, ($\Phi \leq 1$)) for the non-wetted state. Compared with the one-scale structured surface, the solid–liquid contact area at the hierarchical structured surface change from $\Phi_s \times A$ to $\Phi_s \times \Phi_s \times A$ due to the similarity between the primary and secondary structures.[33] Thus, the solid–liquid contact area at the hierarchical structured surface increases from $r_w \times A$ to $r_w \times r_w \times A$ at the fully wetted state but decreses from $\Phi \times A$ to $\Phi \times \Phi \times A$ at the non-wetted state, and depends on the effective wetting ratio f at the partial wetted state. However, the determination of wetting state and effective wetting ratio at the structured surface is still not clear, and the study of effective wetting area is open for questions.

Electrochemical impedance spectroscopy (EIS) is a practical technique applied in numerous fields, especially in surface science.[34-38] EIS provides useful solid–liquid interfacial information based on the signal response under sinusoidal potential excitation at different frequencies.[39-43] In this work, the effective wetting area at structured surface was studied. Nano/microstructures were

prepared on aluminum (Al) surfaces and the static contact angles were measured experimentally. The electrochemical impedance at hydrophilic Al surfaces was evaluated to investigate the solid–liquid contact area. Moreover, the theoretical wetting models were first applied to the equivalent electrical circuits for the electrochemical impedance analysis to estimate the effective wetting area at the structured surface.

EXPERIMENTAL SECTION

Sample Preparation. Chemical etching was used to prepare hydrophilic samples with nano/microstructured surfaces. Al substrates (3003 Al alloy, 20 mm × 15 mm × 0.5 mm) that were previously polished using sandpaper were ultrasonically cleaned with acetone and ethanol sequentially for 10 min, and then rinsed in the deionized water (DI). The substrates were then immersed in 1.25 M NaOH for 10 s to remove the aluminum oxide film from the surface. The etching process was performed by immersing the cleaned substrates in a 1 M $CuCl_2$ solution for 1, 2, 5, 10, or 20 s at room temperature, where they underwent the reactions shown in Eqs. (1) and (2). These samples were designated (b)–(f), respectively, with an unetched control sample being designated (a).

$$2Al + 3CuCl_2 \rightarrow 3Cu + 2AlCl_3 \quad (1)$$

$$2Al + 6H^+ \rightarrow 3H_2 + 2Al^{3+} \quad (2)$$

Here, Cu^{2+} reacts with Al via a replacement reaction, resulting in a thin layer of Cu being deposited on the Al surface. The thin layer of Cu deposition was clearly eliminated by the ultrasonic bath of the DI water, and only Al was observed on the surface (Figure S1) using X-ray diffraction (D8 ADVANCE, Bruker, Germany).

The surface morphology was obtained using the scanning electron microscope (SEM, S−3500N, Hitachi, Japan) and confocal laser scanning microscope (CLSM, LEXT OLS 3000, Olympus, Japan). Liquid droplets (3.5 wt% NaCl solution) of 5 μL were gently deposited on the sample surface with a syringe and the side view images of the droplets were obtained with a digital camera (Figure S2). The average static WCA was determined at six different spots on two sides of each sample at room temperature.

Electrochemical Measurements. The electrochemical properties of the samples were investigated by EIS using an electrochemical workstation (CHI660E, CH Instruments, China). The electrochemical measurements were performed in a three-electrode system comprising a saturated calomel electrode as the reference electrode, a platinum wire as the counter electrode, an Al sample with an exposed surface area of 3.9 cm^2 (15 mm × 13 mm × 2 sides) as the working electrode, and a 3.5 wt% NaCl solution as the electrolyte. Prior to the electrochemical measurements, the sample was immersed in the electrolyte for 60 min to obtain a stable open circuit potential (OCP). A sinusoidal perturbation signal of 5 mV amplitude was then applied, and the impedance spectra were recorded at OCP in the frequency range 0.1 Hz–100 kHz using a logarithmic sweep. The electrochemical data were analyzed with the aid of CHI660E, Zsimpwin, and Zview (Scribner Associates Inc.) software.

RESULTS AND DISCUSSION

Surface Morphology and Wettability. Figure 1 shows SEM images of the fabricated samples (a)–(f). Polishing traces can be observed on the bare Al surface, as shown in Figure 1a, and porous layers containing nano/microstructures are observed on the chemically etched Al surfaces, as shown in Figures 1b–1f. It seems that increasing the chemical etching time results in denser

nano/microstructures. After 1 s immersion, several microscale square cavities are generated on the surface (Figure 1b). When etching time was extended to 2 s and above, the surface morphology changed drastically and the upper layer of surface is found to have damaged. As etching time prolonged to 5 s, geometrical microconvex plate structures are formed on the surface shown in Figure 1d. Furthermore, denser smaller submicro/nano structures start to generated on the top of microconvex plate (yellow dash circle in Figure 1d) but parts of the surfaces are not etched completely (red dash circle in Figure 1d). By extending the etching time to 10 and 20 s, the generated microconvex plate structures were further etched and hierarchically structures were formed on the surfaces shown in Figures 1e and 1f.

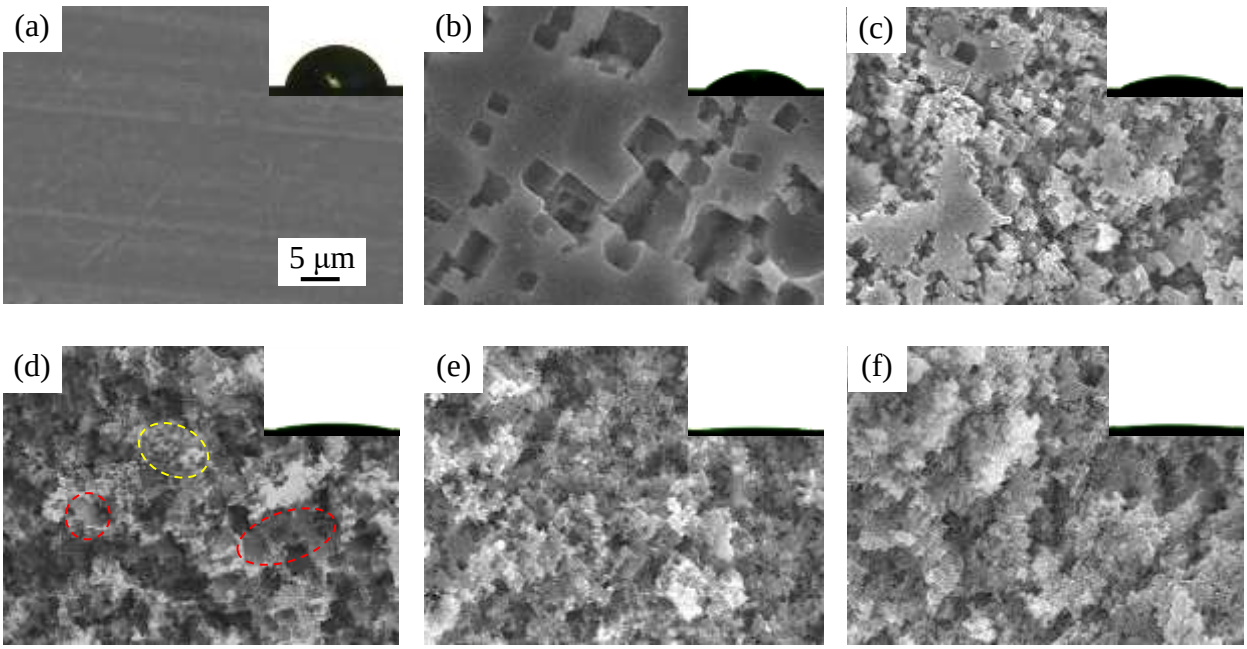

Figure 1. SEM images of Al surfaces after immersed in a $CuCl_2$ solution for (a) 0, (b) 1, (c) 2, (d) 5, (e) 10, and (f) 20 s. The insets show the side views of water droplets on the structured surfaces.

Side views of droplets are also shown in Figure 1. The WCA for a bare Al surface is 77.29° ± 2.06°, and surface hydrophilicity is enhanced with increasing chemical etching time. The WCA is

35.23° ± 0.65° for sample (b), 23.86° ± 1.06° for sample (c), 12.45° ± 1.60° for sample (d), 6.80 ± 1.29° for sample (e) and 4.13 ± 0.79° for sample (f). The static contact angle decreases with increasing chemical-etching time, while the contact radius increases in an opposite manner. Furthermore, arithmetic surface roughness (Ra) were assessed from the cross-sectional profiles (Figure S3). The roughness of the surfaces, which is related to wettability, increases with etching time. The average values of Ra for samples (a)–(f) are 0.254 ± 0.039, 0.809 ± 0.090, 1.002 ± 0.112, 1.942 ± 0.053, 1.969 ± 0.034, and 2.230 ± 0.017 μm, respectively, indicating that denser nano/microstructures are formed with longer etching time.

Electrochemical Analysis. EIS was used to analyze the interfacial electrical impedance of the samples. Typical Nyquist plots, which represent impedance as a complex number with its real part in the x-axis and imaginary part in the y-axis, are shown in Figure 2. The impedance of the bare Al sample with a WCA of 77.79° is the highest, whereas that of the sample etched for 20 s, which has a WCA of 4.13°, is the lowest. That is, electrochemical impedance is correlated with wettability and decreases as WCA decreases.

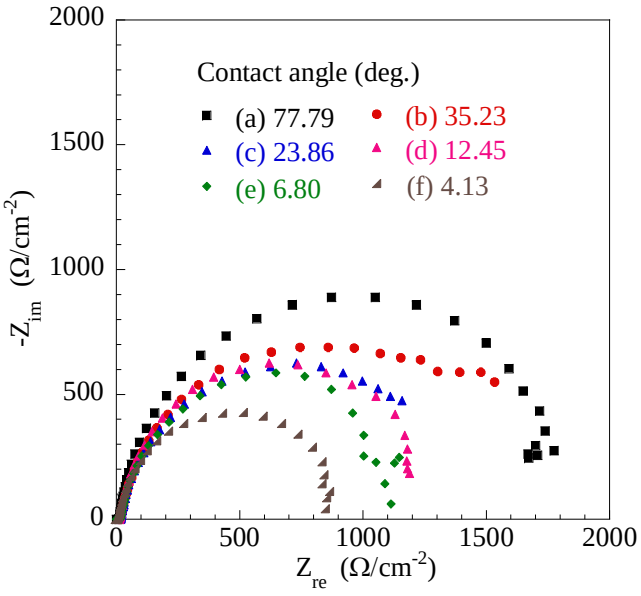

Figure 2. Nyquist plots for Al surfaces with the contact angle of 77.79°, 35.23°, 23.86°, 12.45°, 6.80°, and 4.13° in 3.5 wt% NaCl solution.

Since the defects or inhomogeneities of the electrode surface cause the capacitance components deviate from ideal (smooth) pure capacitance, the Nyquist plots shown in Figure 2 change from semi-circles to semi-ellipses. In order to clarify the effect of effective wetting area on the electrochemical impedance, an EEC with one time constant shown in Figure 3a and 3b was applied to analyze the measured EIS data of the flat and fully wetted structured surfaces. Here R_s is the solution resistance, which is dominated by the electrolyte at a given working electrode surface; C_{dl} is the double-layer capacitance related to the surface structure depending on frequency; and R_{ct} is the charge transfer resistance determined by the surface conductivity and the polarization resistance.[44]

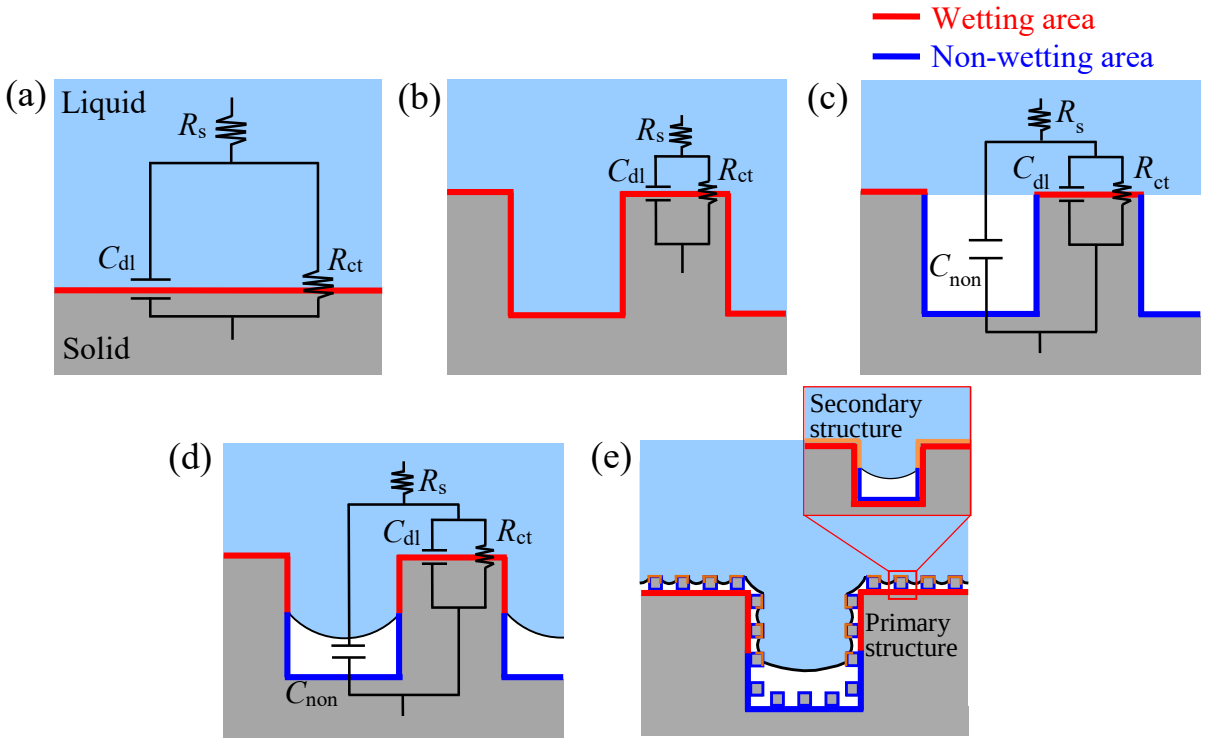

Figure 3. Schematic views and equivalent electrical circuits (EECs) for the solid–liquid interfaces of different samples immersed in NaCl solutions: (a) flat surface, (b) fully wetted structured surface, (c) non-wetted structured surface, (d) partial wetted structured surface and (e) partial wetted hierarchically structured surface.

Compared to the EECs shown in Figures 3a and 3b, a capacitance is added to the non-wetting area, C_{non}, as a parallel element for the non-wetted and partial wetted structured surface. Therefore, the total equivalent impedance is derived from a parallel combination of the wetted area and the non-wetted area impedances. Figures 3c and 3d show the schematics of solid–liquid interface and the corresponding EECs of non-wetted and partial wetted one-scale structured surfaces, and Figure 3e shows that of the hierarchically structured surface. Remarkably, under normal temperature and pressure, the electronic and ionic conductivity of non-wetting area (air or vacuum) is almost 0, which is much smaller than that of electrolyte (NaCl solution). Thus, the electrons and ions cannot easily pass through the non-wetting area, resulting in the impedance modulus of non-wetting area is much larger than that of wetting area ($|Z_{\text{wetting}}| \ll |Z_{\text{non-wetting}}|$). As the total equivalent impedance dependent on the lower impedance at the parallel circuits, which indicate that the solid–liquid contact area plays dominate role in the impedance measurement. As a result, the EECs of the non-wetted and partial wetted structured surfaces can be simplified to that shown in Figure 3a.

Considering the defects or inhomogeneities of the samples, a constant phase element (CPE) is used to fit the non-ideal capacitive behavior instead of the electrical capacitance C_{dl}, for the one time constant EEC. The impedance of the CPE (Z_{CPE}) is

$$Z_{\text{CPE}} = \frac{1}{Q(\mathrm{j}\omega)^{n}} \tag{3}$$

where j is a unit of the imaginary part ($j = \sqrt{-1}$), ω is the angular frequency, $\omega = 2\pi f$ (rad/s), n is an exponential coefficient, and Q is a constant.[45,46] Therefore, the impedance Z becomes

$$Z = R_s + \frac{R_{ct}}{R_{ct}Q(j\omega)^n + 1} \quad (4)$$

Table 1. Electrochemical data for samples in a 3.5 wt% NaCl solution.

Samples	R_s ($\Omega \cdot cm^2$)	CPE		R_{ct} ($\Omega \cdot cm^2$)
		Q (Ω^{-1} s^n/cm^2)	n	
a	12.5	1.517×10^{-5}	0.930	1905.3
b	15.5	1.201×10^{-4}	0.887	1753.0
c	17.4	6.884×10^{-5}	0.900	1461.5
d	13.9	3.903×10^{-5}	0.919	1385.7
e	15.0	3.888×10^{-5}	0.861	1242.5
f	11.5	4.872×10^{-5}	0.913	960.3

The comparison of Nyquist plots simulated by CPE and that of C_{dl} for bare Al are shown in Figure 4. The CPE (red line) and C_{dl} plots (blue line) agree well with the experimental results, and no significant difference was observed. Table 1 summarizes the data analyzed for each sample. The value of n can be approximated to 1 with a range of 0.861–0.930. Also, the simulated results

of CPE and C_{dl} for the etched samples show tendencies similar to those for the bare Al, which is in agreement with the experimental results (Figure S4). Thus, the CPE shows capacitor behavior and can be replaced by C_{dl}.

As the impedance spectra were recorded in the frequency range of 0.1 Hz–100 kHz, the influence of frequency on impedance was investigated. At low frequency region, since the wavelength of the disturb signal is long, the ions, electrons are difficult to penetrate the solid–vapor–liquid interface (blue parts in Figure S5a). The charge only transfers at the solid–liquid contact area. On the other hand, the wavelength is short at high frequency region (Figure S5b), ions and electrons are easy to obtain energy, which result in large penetration force. Thus, there is no significant deviation of charge transfer between the solid–liquid interface and solid–vapor–liquid interface. As a result, the impedance at low frequency region was studied to better clarify the effective wetting area at the structured surfaces.

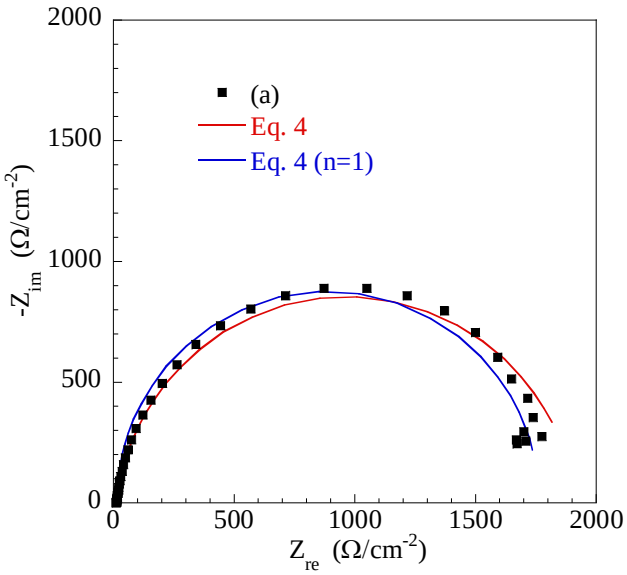

Figure 4. Nyquist plots of the experimental data and those derived from Eq. (4) for the sample (a).

Based on the EEC shown in Figure 3a, the impedance Z and the modulus of impedance $|Z|$ are given by Eqs. (5) and (6), respectively,

$$Z = R_s + \frac{R_{ct}}{1 + j\omega R_{ct} C_{dl}} \tag{5}$$

$$|Z| = \sqrt{R_s^2 + \frac{R_{ct}^2 + 2R_{ct}R_s}{1 + (R_{ct}\omega C_{dl})^2}} \tag{6}$$

The term $(R_{ct}\omega C_{dl})^2$ is small enough to be neglected at low frequency.[47] Thus, $|Z|$ is

$$|Z| = R_s + R_{ct}\,, \tag{7}$$

where $|Z| \approx R_{ct}$ if $R_s \ll R_{ct}$. Defining Z_0 as the impedance of flat bare Al surface (apparent area (A_0) = 3.9 cm^2), the real contact area can be obtained as follows:

$$A = \frac{|Z_0|}{|Z|} A_0 \tag{8}$$

Table 2. Impedance elements at low frequency and real contact area.

Samples	$\|Z\|$ (Ω·cm^2)	R_{ct} (Ω·cm^2)	$\|Z_{C_{dl}}\|$ (Ω·cm^2)	R_s (Ω·cm^2)	A/A_0 (-)	A (cm^2)
a	1917.8	1905.3	1.104×10^4	12.5	1.00	3.90
b	1768.5	1753.0	1.325×10^3	15.5	1.08	4.21
c	1478.9	1461.5	2.331×10^3	17.4	1.30	5.07

d	1399.5	1385.7	4.078×10^3	13.9	1.37	5.34
e	1257.6	1242.5	4.093×10^3	15.0	1.53	5.97
f	971.9	960.3	3.267×10^3	11.5	1.97	7.68

Table 2 shows the analysis results based on EIS data for the low frequency of 0.1 Hz. The impedance modulus $|Z|$ is almost equal to R_{ct}, and R_s is small enough to be ignored. The impedance of C_{dl} is large at low frequency; however, it can be ignored because it is a parallel element in the EECs. We confirm that R_{ct} is the dominant factor for $|Z|$ at low frequency. Furthermore, the real contact areas for the partial wetting model were estimated and, as shown in Table 2, the effective wetting area increases with decreasing contact angle. The ratio of the real contact area to the apparent area for the sample etched for 20 s is close to 1.97 owing to the denser nano/microstructures, as shown in Figure 1f. As shown in Figure 5, the total impedance modulus and R_{ct} show a similar correlation with the WCA at low frequency, i.e., a surface with a larger WCA has a larger impedance and smaller effective wetting area. Moreover, compared to other elements shown in EECs, R_{ct} is found to be the dominant parameter at low frequency and can be used to estimate the effective wetting area.

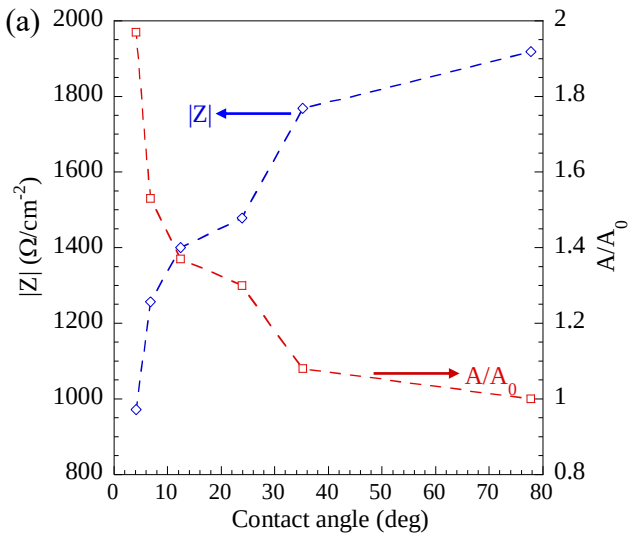

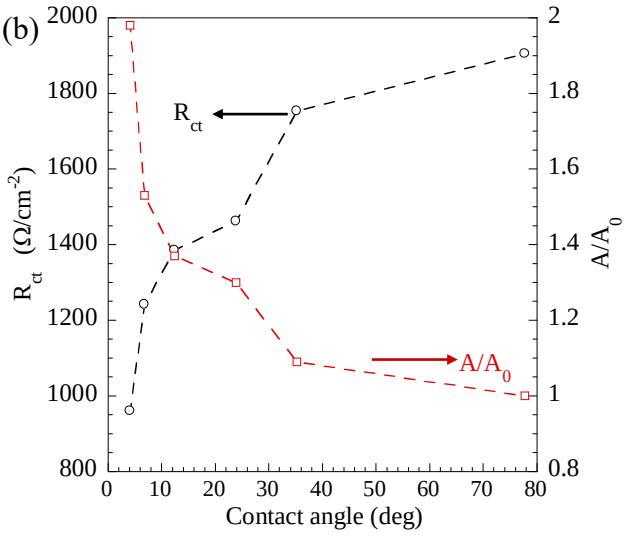

Figure 5. Effect of contact angle on electrochemical property and real contact area: (a) impedance modulus and (b) charge transfer resistance (the dotted lines are eye guides).

CONCLUSION

The effective wetting area of the solid–liquid interface at the nano/microstructured surface was investigated on the basis of the electrochemical impedance analysis in this study. We first applied the theoretical wetting model to the equivalent electrical circuits for the electrochemical

impedance analysis to estimate the effective wetting area of hydrophilic nano/microstructured surfaces. The water contact angle decreases significantly at hydrophilic surfaces with denser nano/microstructures. The electrochemical impedance decreases with reducing water contact angle, showing a dependence on the effective wetting area at the solid–liquid interface. Also, the charge transfer resistance at a low frequency is the most important factor to estimate the effective wetting area at the solid–liquid interface. Further experiments and electrochemical analysis on the effective wetting area at the hydrophobic nano/microstructured surfaces are now under investigation.

DISCLOSURE

The authors declare no competing financial interest.

ACKNOWLEDGMENT

D. J. Z. would like to appreciate Professor Changsong Liu, Qingdao University of Technology for the use of electrochemical impedance measurement. This work is partly supported by the Ministry of Education, Science and Culture of the Japanese Government through the Grant-in Aid for Scientific Research, Project No. 18H01385 and No. 21360099, the research foundation of Kyushu Institute of Technology, and the Initiative for Realizing Diversity in the Research Environment by Ministry of Education, Culture, Sports, Science and Technology, Japan.

REFERENCES

(1) Rafiee, J.; Mi, X.; Gullapalli, H.; Thomas, A. V.; Yavari, F.; Shi, Y.; Ajayan, P. M.; Koratkar, N. A. Wetting Transparency of Graphene. *Nat. Mater.* **2012**, *11*, 217–222.

(2) Tian, Y.; Su, B.; Jiang, L. Interfacial Material System Exhibiting Superwettability. *Adv. Mater*. **2014**, *26*, 6872–6897.

(3) Yao, X.; Song, Y.; Jiang, L. Applications of Bio-inspired Special Wettable Surfaces. *Adv. Mater*. **2011**, *23*, 719–734.

(4) Bellanger, H.; Darmanin, T.; Taffin de Givenchy, E.; Guittard, F. Chemical and Physical Pathways for the Preparation of Superoleophobic Surfaces and Related Wetting Theories. *Chem. Rev*. **2014**, *114*, 2694–2716.

(5) Basu, B. J.; Manasa, J. Effect of Deposition Parameters on the Wettability and Microstructure of Superhydrophobic Films with Hierarchical Micro–nano Structures. *J. Colloid Interface Sci.* **2011**, *363*, 655–662.

(6) Whitesides, G. M. The Origins and the Future of Microfluidics. *Nature* **2006**, *442*, 368–373.

(7) Liu, Z.; Zhao, J. W.; Xu, W. Y.; Qian, L.; Nie, S.H.; Cui, Z. Effect of Surface Wettability Properties on the Electrical Properties of Printed Carbon Nanotube Thin-Film Transistors on SiO_2/Si Substrates. *ACS Appl. Mater. Interfaces* **2014**, *6*, 9997–10004.

(8) Zhang, J.; Kwok, D. Y. Contact Line and Contact Angle Dynamics in Superhydrophobic Channels. *Langmuir* **2006**, *22*, 4998–5004.

(9) Liu, Q.; Chen, D. X.; Kang, Z. X. One-step Electrodeposition Process to Fabricate Corrosion-resistant Superhydrophobic Surface on Magnesium Alloy. *ACS Appl. Mater. Interfaces* **2015**, *7*, 1859–1867.

(10) Ohba, T.; Yamamoto, S.; Kodaira, T.; Hata, K. Changing Water Affinity from Hydrophobic to Hydrophilic in Hydrophobic Channels. *Langmuir* **2015**, *31*, 1058–1063.

(11) Raj, R.; Maroo, S. C.; Wang, E. N. Wettability of Graphene. *Nano Lett.* **2013**, *13*, 1509–1515.

(12) Bocquet, L.; Lauga, E. A Smooth Future?. *Nat. Mater.* **2011**, *10*, 334–337.

(13) Kandlikar, S. G. History, Advances, and Challenges in Liquid Flow and Flow Boiling Heat Transfer in Microchannels: A Critical Review. *J. Heat Transfer* **2012**, *134*, 034001.

(14) Wang, X. Q.; Mujumdar, A. S. Heat Transfer Characteristics of Nanofluids: A Review. *Int. J. Therm. Sci*. **2007**, *46*, 1–19.

(15) Nagayama, G.; Matsumoto, T.; Fukushima, K.; Tsuruta, T. Scale Effect of Slip Boundary Condition at Solid–liquid Interface. *Sci. Rep.* **2017**, *7*, 43125.

(16) Fang, C.; David, M.; Wang, F. M.; Goodson, K. E. Influence of Film Thickness and Cross-sectional Geometry on Hydrophilic Microchannel Condensation. *Int. J. Multiph. Flow* **2010**, *36*, 608–619.

(17) Grimaldi, J.; Radhakrishna, M.; Kumar, S. K.; Belfort, G. Stability of Proteins on Hydrophilic Surfaces. *Langumir* **2014**, *31*, 1005–1010.

(18) Koňák, C.; Šubr, V.; Kostka, L.; Štěpánek, P.; Ulbrich, K.; Schlaad, H. Coating of Vesicles with Hydrophilic Reactive Polymers. *Langmuir* **2008**, *24*, 7092–7098.

(19) Jin, C.; Qu, Y.; Wang, M.; Han, J.; Hu, Y.; Guo, R. Aqueous Solution-Based Fe_3O_4 Seed-Mediated Route to Hydrophilic Fe_3O_4–Au Janus Nanoparticles. *Langmuir* **2016**, *32*, 4595–4601.

(20) Drelich, J.; Chibowski, E. Superhydrophilic and Superwetting Surfaces: Definition and mechanisms of Control. *Langmuir* **2010**, *26*, 18621–18623.

(21) Cheng, Y; Lu, S.; Xu, W. Controllable Wettability of Micro-and Nano-dendritic Structures Formed on Aluminum Substrates. *New J. Chem.* **2015**, *39*, 6602–6610.

(22) Teisala, H.; Tuominen, M.; Aromaa, M.; Stepien, M.; Mäkelä, J. M.; Saarinen, J. J.; Toivakka, M.; Kuusipalo, J. Nanostructures Increase Water Droplet Adhesion on Hierarchically Rough Superhydrophobic Surfaces. *Langmuir* **2012**, *28*, 3138–3145.

(23) Mammen, L.; Deng, X.; Untch, M.; Vijayshankar, D.; Papadopoulos, P.; Berger, R.; Riccardi, E.; Leroy, F.; Vollmer, D. Effect of Nanoroughness on Highly Hydrophobic and Superhydrophobic Coatings. *Langmuir* **2012**, *28*, 15005–15014.

(24) Weibel, D. E.; Michels, A. F.; Feil, A. F.; Amaral, L.; Teixeira, S. R.; Horowitz, F. Adjustable Hydrophobicity of Al Substrates by Chemical Surface Functionalization of Nano/microstructures. *J. Phy. Chem. C* **2010**, *114*, 13219–13225.

(25) Onda, T.; Shibuichi, S.; Satoh, N.; Tsujii, K. Super-water-repellent Fractal Surfaces. *Langmuir* **1996**, *12*, 2125–2127.

(26) Wenzel, R. N. Resistance of Solid Surfaces to Wetting by Water. *Ind. Eng. Chem. Res.* **1936**, *28*, 988–994.

(27) Cassie, A. B. D.; Baxter, S. Wettability of Porous Surfaces. *Trans. Faraday Soc.* **1944**, *40*, 546–551.

(28) Nagayama, G.; Shi-iki, S.; Tsuruta, T. Effects of Nanostructures on Surface Wettability: A Molecular Dynamics Study. *Trans Japan Soc. Mech. Eng. B* **2007**, *73*, 1084–1091.

(29) Yang J.; Wang, J.; Wang, C.W.; He, X.; Li, Y.; Chen, J.B.; Zhou, F. Intermediate wetting states on nanoporous structures of anodic aluminum oxide surfaces. *Thin Solid Films* **2014**, *562* 353–360.

(30) Wang, G.; Jia, Z. H.; Yang, H. N. Stability of a water droplet on micropillared hydrophobic surfaces. *Colloid Polym. Sci.* **2016**, *294*, 851–858.

(31) Liu, Y.; Choi, C. H. Condensation-induced wetting state and contact angle hysteresis on superhydrophobic lotus leaves. *Colloid. Polym. Sci.* **2013**, *291*, 437–445.

(32) Nagayama, G.; Mizumoto, K.; Yui, R.; Tsuruta, T. Effect of Nano/Microstructures on Wetting Behavior of a Droplet. *Proc. 4th Int. Sympo. Micro Nano Tech.* **2013**, *125*, 1–14.

(33) Nagayama, G., Zhang, D. J. Wetting at Micro/nano-structured Surfaces: Intermediate State between Wenzel and Cassie–Baxter States. submitted for publication.

(34) Lasia, A. *Electrochemical Impedance Spectroscopy and its Applications*, 1–5, New York: Springer-Verlag, **1999**.

(35) Drüschler, M.; Borisenko, N.; Wallauer, J.; Winter, C.; Huber, B.; Endres, F.; Roling, B. New Insights into the Interface Between a Single-crystalline Metal Electrode and an Extremely Pure Ionic Liquid: Slow Interfacial Processes and the Influence of Temperature on Interfacial Dynamics. *Phys. Chem. Chem. Phys.* **2012**, *14*, 5090–5099.

(36) Stoller, M. D.; Park, S.; Zhu, Y.; An, J.; Ruoff, R. S. Graphene-based Ultracapacitors. *Nano Lett.* **2008**, *8*, 3498–3502.

(37) Boinovich, L.B.; Gnedenkov, S. V.; Alpysbaeva, D. A.; Egorkin, V. S.; Emelyanenko, A. M.; Sinebryukhov, S. L.; Zaretskaya, A. K. Corrosion Resistance of Composite Coatings on Low-carbon Steel Containing Hydrophobic and Superhydrophobic Layers in Combination with Oxide Sublayers. *Corros. Sci.* **2011**, *55*, 238–245.

(38) Díaz, B.; Härkönen, E.; Światowska, J.; Mauricea, V.; Seyeuxa, A.; Ritalac, M.; Marcusa, P. Low-temperature Atomic Layer Deposition of Al_2O_3 Thin Coatings for Corrosion Protection of Steel: Surface and Electrochemical Analysis. *Corros. Sci.* **2011**, *53*, 2168–2175.

(39) Mansfeld, F. Use of Electrochemical Impedance Spectroscopy for the Study of Corrosion Protection by Polymer Coatings. *J. Appl. Electrochem.* **1995**, *25*, 187–202.

(40) Largeot, C.; Portet, C.; Chmiola, J.; Taberna, P. L.; Gogotsi, Y.; Simon, P. Relation Between the Ion Size and Pore Size for an Electric Double-layer Capacitor. *J. Am. Chem. Soc.* **2008**, *130*, 2730–2731.

(41) Pan, J.; Thierry, D.; Leygraf, C. Electrochemical Impedance Spectroscopy Study of the Passive Oxide Film on Titanium for Implant Application. *Electrochim. Acta* **1996**, *41*, 1143–1153.

(42) Gnedenkov, S. V.; Sinebryukhov, S. L.; Egorkin, V. S.; Mashtalyar, D. V.; Alpysbaeva, D. A.; Boinovich, L. B. Wetting and Electrochemical Properties of Hydrophobic and Superhydrophobic Coatings on Titanium. *Colloids Surf., A* **2001**, *383*, 61–66.

(43) Corso, B. L.; Perez, I.; Sheps, T.; Sims, P. C.; Collins, P. G. Electrochemical Charge-Transfer Resistance in Carbon Nanotube Composites. *Nano Lett.* **2014**, *14*, 1329–1336.

(44) Chang, B. Y.; Park, S. M. Electrochemical Impedance Spectroscopy. *Annu. Rev. Anal. Chem.* **2010**, *3*, 207–229.

(45) Qian, M.; Soutar, A. M.; Tan, X. H.; Xian, T. Z.; Wijesinghe, S. L. Two-part Epoxy-siloxane Hybrid Corrosion Protection Coatings for Carbon Steel. *Thin Solid Films* **2009**, *517*, 5237–5242.

(46) Chen, S.; Chen, Y.; Lei, Y.; Yin, Y. Novel Strategy in Enhancing Stability and Corrosion Resistance for Hydrophobic Functional Films on Copper Surfaces. *Electrochem. Commun.* **2009**, *11*, 1675–1679.

(47) Martini, E. M. A.; Muller, I. L. Characterization of the Film Formed on Iron in Borate Solution by Electrochemical Impedance Spectroscopy. *Corros. Sci.* **2000**, *42*, 443–454.

1 Graphic Abstract

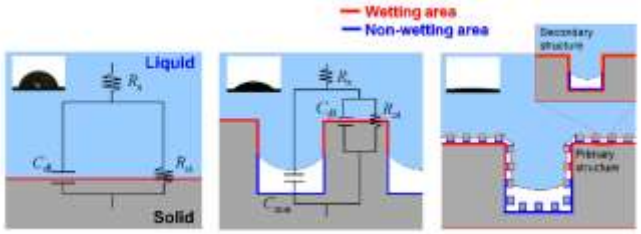

2